RESEARCH ARTICLE

WILEY **NMR** IN BIOMEDICINE

Multiparametric MR for non-invasive evaluation of tumour tissue histological characteristics after radionuclide therapy

Mikael Montelius[1] 🔾 | Oscar Jalnefjord[1,2] | Johan Spetz[1] | Ola Nilsson[3] | Eva Forssell-Aronsson[1] | Maria Ljungberg[1,2]

[1] Institute of Clinical Sciences, Sahlgrenska Cancer Center, Sahlgrenska Academy, Department of Radiation Physics, University of Gothenburg, Gothenburg, Sweden

[2] Department of Medical Physics and Biomedical Engineering, Sahlgrenska University Hospital, Gothenburg, Sweden

[3] Institute of Biomedicine, Sahlgrenska Cancer Center, Sahlgrenska Academy, Department of Pathology, University of Gothenburg, Gothenburg, Sweden

Correspondence
Mikael Montelius, Department of Radiation Physics, Institute of Clinical Sciences, University of Gothenburg, MR centre, Bruna stråket 13, 413 45 Gothenburg, Sweden.
Email: mikael.montelius@radfys.gu.se

Early non-invasive tumour therapy response assessment requires methods sensitive to biological and physiological tumour characteristics.

The aim of this study was to find and evaluate magnetic resonance imaging (MRI) derived tumour tissue parameters that correlate with histological parameters and that reflect effects of radionuclide therapy.

Mice bearing a subcutaneous human small-intestine neuroendocrine tumour were *i.v.* injected with ^{177}Lu-octreotate. MRI was performed (7 T Bruker Biospec) on different post-therapy intervals (1 and 13 days) using T2-weighted imaging, mapping of T2* and T1 relaxation time constants, as well as diffusion and dynamic contrast enhancement (DCE-MRI) techniques. After MRI, animals were killed and tumours excised. Four differently stained histological sections of the most central imaged tumour plane were digitized, and segmentation techniques were used to produce maps reflecting fibrotic and vascular density, apoptosis, and proliferation. Histological maps were aligned with MRI-derived parametric maps using landmark-based registration. Correlations and predictive power were evaluated using linear mixed-effects models and cross-validation, respectively.

Several MR parameters showed statistically significant correlations with histological parameters. In particular, three DCE-MRI-derived parameters reflecting capillary function additionally showed high predictive power regarding apoptosis (2/3) and proliferation (1/3). T1 could be used to predict vascular density, and perfusion fraction derived from diffusion MRI could predict fibrotic density, although with lower predictive power.

This work demonstrates the potential to use multiparametric MRI to retrieve important information on the tumour microenvironment after radiotherapy. The non-invasiveness of the method also allows longitudinal tumour tissue characterization. Further investigation is warranted to evaluate the parameters highlighted in this study longitudinally, in larger studies, and with additional histological methods.

KEYWORDS

cancer, functional MRI, histopathology, IVIM, tumour therapy response

1 | INTRODUCTION

Neuroendocrine tumours (NETs) are slow-growing malignancies and metastases are often found at the time of diagnosis. Currently available treatment options have limited effect on patient survival. New therapeutic options are being developed, such as radionuclide therapy (RNT) using the radiolabelled somatostatin analogue octreotate (^{177}Lu-octreotate). This compound binds to receptors expressed on tumour cells. Thereby the radiation dose to primary and metastatic tumours is maximized, while exposure of healthy tissue to radiation is limited. ^{177}Lu-octreotate shows great potential for treatment of NETs, but optimization of therapy protocols is required. To facilitate this, non-invasive methods for prediction and assessment of therapeutic effects are needed.

Tumour size is conventionally regarded as a response endpoint. It can be accurately determined using computed tomography (CT) or magnetic resonance (MR) imaging, but is becoming obsolete for evaluating modern, targeted therapies. Methods that are sensitive to the targeted biological processes, such as angiogenesis, proliferation and apoptosis are required instead.[1-3]

Histological methods provide unambiguous characterization of biological features of tumours, but examining an entire tumour precludes longitudinal assessment, while biopsies only provide information on the focally sampled tissue regions. Erroneous sampling and problematic anatomical locations of tumours are further limiting factors.

Several functional MR imaging methods are currently being investigated for their ability to indirectly measure tumour characteristics. Promising results regarding early assessment of tumour response to RNT have been found.[1,4] For example, dynamic contrast-enhanced MR imaging (DCE-MRI) is used in oncological imaging to reveal abnormal biokinetic interactions between tumour tissue and contrast material. Semi-quantitative or quantitative parametric analysis or modelling of the DCE-MRI signal-time curve can provide important information on, *e.g.*, spatial distribution of vascularity, vessel structure and function, oxygenation, perfusion, and blood volume.[5] Diffusion weighted MRI (DWI) is commonly used to measure structural restrictions on the Brownian motion of tissue water molecules. Measures obtained can exclude (diffusion coefficient, D) or include (apparent diffusion coefficient, ADC) perfusion related water molecule motion. In addition, DWI can be used to determine the fractional tissue volume of actively perfused microvasculature (f).[6] Quantification of magnetic relaxation times ($T1$, $T2$, and $T2^*$) can reveal altered molecular organization, presence of macromolecules after microvasculature restructuring or leakage, or changes in tissue deoxyhaemoglobin levels.[7,8]

Furthermore, the interest in combining several MR techniques in a multiparametric MR (mpMR) approach is increasing, since it would enable a non-invasive, spatiotemporally resolved, comprehensive evaluation of several dynamic and functional biological mechanisms that are associated with tumour response.[1,9-12]

In previous studies, individual MR-derived tissue parameters for tumour response assessment (*e.g.* water diffusion, vascular parameters, perfusion and hypoxia) have been correlated with biological measures. However, the results sometimes show weak, diverging or even contradictory results, most likely due to the diversity of tumour types, therapeutic modalities, experimental conditions and methodologies described in the literature.[13,14] Hence, developing a reliable and sensitive response assessment method based on mpMR necessitates a comprehensive evaluation of the link between the pathophysiological processes and the MR-derived tissue parameters for each combination of tumour type and treatment modality studied.

For MR-derived parameters to provide robust *in vivo* tumour therapy response assessment, the MR-methods must be better optimized and understood, both regarding acquisition and evaluation of data, and the parameters must be evaluated with corresponding histological tissue data (*e.g. Dominietto & Rudin, 2013*[11]). To our knowledge, the biological interpretation of mpMR data of NETs receiving RNT has not been studied using histological methods.

2 | AIM

The aim of this project was to evaluate the potential of mpMR for response assessment of NETs receiving RNT by studying correlations between *in vivo*, MR-derived tissue parameters and biological characteristics of corresponding *ex vivo* tissue samples.

3 | MATERIALS & METHODS

3.1 | Tumour model and therapeutics

Samples from the human small-intestine neuroendocrine tumour model (GOT1[15]) were xenografted subcutaneously on female BALB/c nude mice (n = 21, Charles River, Wilmington, MA, USA) that were fed with a standard diet and water *ad libitum*. Each animal grew one tumour in the neck region, which will be referred to as tumour 1 for animal 1, tumour 2 for animal 2, etc. As tumours reached 10–20 mm in diameter, 15 MBq ^{177}Lu-octreotate (specific activity: 26 MBq/µg octreotate, IDB Holland, Baarle-Nassau, the Netherlands) was injected intravenously, resulting in an absorbed dose to the tumour of approximately 4 Gy (cf. Dalmo *et al.*, 2017[16]). The initial 21 animals were included in our mpMR project, including studies on the longitudinal behaviour of MR-derived tissue parameters in response to therapy[4] and optimization of image post processing techniques,[17] both with different specific aims and results. Based on inclusion criteria described below, n = 5 of the 21 animals were evaluated in the current study.

The Gothenburg Ethical Committee on Animal Research approved this study.

3.2 | Overall experimental setup

To correlate MRI data with a broad range of biological response effects, rather than with effects from therapeutic doses, and thereby to increase the biological variability of the investigated parameters, we used a non-curative amount of ^{177}Lu-octreotate (15 MBq) and also included data from different time points after treatment.

Imaging experiments including the methods mentioned in Table 1 were conducted on days −1, 1, 3, 8, and 13 after treatment (day 0), whereof data from days 1, 8 and 13 are included in the current study. The T2 weighted images were used to verify partial tumour response (reduced tumour volume or reduced growth rate during the first week after treatment, followed by stable or increasing tumour volume during the second week, data not shown) as previously described.[18]

The 5/21 tumours included in this study fulfilled the following requirements: 1) they were successfully imaged in the MR experiment preceding tumour extraction, 2) they were adequately located, shaped and sized for the resection method used, 3) they were successfully stained at histology, and 4) anatomical landmarks were recognizable on both histological sections and MR images. These inclusion criteria resulted in 4/5 included tumours (no. 1, 3, 4 and 5) being harvested on day 13 and 1/5 included tumours (no. 2) being harvested on day 1.

During imaging, animals were anaesthetized using air and isoflurane (2–3%, MSD Animal Health, Copenhagen, Denmark), body temperature was maintained using a circulating warm water system and a heating pad, and a pressure sensitive pad was used to monitor respiration (SA Instruments, Inc., NY, USA). For contrast-material administration during image acquisition, a peripheral venous catheter was fixed to the tail vein and connected to a 1 ml syringe outside the magnet bore via a 70 cm infusion line.

Immediately after the MRI experiment preceding the tumour extraction, animals received a lethal intraperitoneal injection of sodium pentobarbitone (Pentobarbitalnatrium vet, Apotek Produktion & Laboratorier AB, Huddinge, Sweden, 60 mg/ml) followed by heart incision, tumour extraction and histological preparation.

3.3 | MRI experiments

MRI examinations were performed using a 20-cm inner-diameter horizontal bore 7 T MR system with 400 mT/m gradients (Bruker BioSpin MRI GmbH, Ettlingen, Germany; software: ParaVision 5.1).

TABLE 1 MR examinations and pulse sequence parameters

MR technique & pulse sequence	Pulse sequence parameters
IVIM-DWI	3 orthogonal gradient directions, gradient separation/duration: 9/4 ms 12 b-values: 0, 5, 10, 20, 35, 50, 75, 100, 200, 400, 600 and 800 s/mm^2
2D SE-EPI	TR: 1500 ms, TE: 21 ms, number of averages/segments: 3/1 Effective bandwidth $\approx$ 300 kHz Partial Fourier acceleration: 1.5 Pixel size: 320^2 μm^2, slice thickness: 1000 μm, slice gap: 500 μm Fat suppression: Frequency selective Scan time < 6 minutes
T2*-mapping	10 echoes (TE): 5, 10, 15, ... 50 ms TR: 2000 ms, number of averages: 1, flip angle: 30°
Multiple echo gradient echo (MGE)	Slice positions imported from IVIM-DWI experiment Pixel size: 160^2 μm^2, slice thickness: 1000 μm No fat suppression scan time < 4 minutes
T1-mapping	7 TR: 13000, 9000, 4500, 2500, 1500, 750, 300 ms TE: 24 ms, number of averages: 1, RARE factor: 4
2D RARE (RAREVTR)	Refocusing flip angle: 180° Pixel size: 280^2 μm^2, slice thickness: 1000 μm, single slice Slice positions imported from IVIM-DWI experiment (central slice) No fat suppression Scan time < 10 minutes
DCE-MRI	Number of repetitions (dynamics): 100, temporal resolution: 4.2 s (varied slightly with FOV), contrast injection during sixth dynamic
2D RARE	TR: 300 ms, TE: 24 ms, number of averages: 1, RARE factor: 4 Partial Fourier acceleration: 1.5 Pixel size: 280^2 μm^2, slice thickness: 1000 μm, single slice Slice positions imported from IVIM-DWI experiment (central slice) Fat suppression: Frequency selective Scan time < 8 minutes
T2 weighted MRI	TR: 4190 ms, TE: 45 ms, number of averages: 2, RARE factor: 6 Pixel size: $(160 \pm 50)^2$ μm^2 (varied with FOV)
2D RARE	Slice thickness: 700 μm, no slice gap Fat suppression: Frequency selective Scan time < 4 min

A 4-channel array rat brain receiver coil (RAPID Biomedical GmbH, Rimpar, Germany) and a 72-mm volume coil were used to image tumours 1 and 3, 4, and 5, and a 50-mm quadrature transmit/receive volume coil was used to image tumour 2 (RAPID Biomedical GmbH, Germany).

Field-map based shimming (MAPSHIM) was used to improve the field homogeneity within the tumour. Transversal images of the longitudinal position of the animal with greatest tumour area were acquired using a field of view (FOV) that covered the tumour extent, including the following methods: Multi b-value diffusion-weighted imaging for intravoxel incoherent motion modelling (IVIM-DWI), $T2^*$ and $T1$ quantification, dynamic contrast-enhanced MRI (DCE-MRI: 0.1 M Gd-DTPA, DOTAREM, Gothia Medical, Billdal, Sweden, 0.3 mmol/kg bodyweight, tail *i.v.* injection during the 6th dynamic) and T2-weighted MRI.

Imaging experiments were performed on the same day the animal was killed for tumour tissue harvesting, except for the DCE-MRI experiments on animals 1, 3, 4, and 5, which were conducted on day 8 instead of day 13 for logistical reasons involving the other studies. Total scan time was approximately 90 min. Detailed acquisition parameters are given in Table 1.

3.4 | MR image post processing

Post processing was performed on a voxel-by-voxel basis using MATLAB (R2015b, The MathWorks, Inc., Natick, MA, USA) with standard and in-house developed functions, scripts and graphical user interfaces. A 2 × 2 median filter was applied to all images for noise reduction before further post-processing. The 19 parameters derived from MRI examinations are defined in Table 2.

3.5 | Tissue sampling, histological processing and digitization

Just after the animal had been killed, a scalpel was used to divide the tumour *in situ* by placing a section adjacent and parallel to the imaged tumour plane. The same plane was colour coded with tissue ink on the left, right, and dorsal tumour borders to keep track of anatomical orientation during histological processing. At paraffin embedding (Thermo Scientific™ HM 355S Automatic, Fisher Scientific, Lund, Sweden), the flat tumour surface made by the scalpel was positioned to meet the sweep plane of the microtome knife. When the tissue ink was reached by the microtome, *i.e.* when the imaged tumour plane was reached, serially produced 3-μm sections were collected for histological and immunohistochemical staining. Digital images of the stained sections were produced using a Leica SCN400 Slide Scanner (40× magnification, Leica Microsystems, Wetzlar, Germany), resulting in images of 0.25 × 0.25 μm² resolution. Image post-processing was performed in MATLAB, where the tissue ink was located on the magnified images, allowing proper alignment of the digitized histological images and the MR images. Figure 1 visualizes the process of producing digital histology images for subsequent alignment with the corresponding MR parameter maps.

Four stains were applied to adjacent tumour sections: haematoxylin-eosin (HE, Tissue-Tek Prisma, Sakura FineTek, Alphen aan den Rijn, the Netherlands), Masson Trichrome (MT, Artisan Link, Dako, Glostrup, Denmark), and antibodies to Ki67 (AB9260; Merck Milipore Burlington, MA, USA) and CD31 (AB28365; Abcam, Cambridge, UK). The latter two were pre-treated with EnVision™ FLEX Target Retrieval Solution (high pH; PT-Link; Dako, Glostrup, Denmark) followed by incubations using Envision Flex (Dako, Glostrup, Denmark). The staining was performed in an Autostainer Link (Dako, Glostrup, Denmark) following the manufacturer's instructions. Positive and negative controls were included in each run.

3.6 | Image registration and data sampling

Landmark-based manual image registration using the MATLAB control point selection tool was performed to intermutually align the histological images and to register them to the T2-weighted MRI. The MR parameter maps were manually registered to the T2-weighted image by manual adjustment of rotation, translation and scaling. The MATLAB *fitgeotrans* function, which fits a geometric transformation to pairs of landmark points defined in the images to be aligned, was then used to infer the transformation matrices linking all images. Tumour regions affected by obvious histological tears/folds or MR-related artefacts, or where landmarks could not be identified were avoided by performing the registration and data sampling sequentially on tumour sub-regions. Figure 2 illustrates how a data sample is taken from a registered tumour sub-region. Before the automatic sampling process of a registered sub-region was started, the histological regions corresponding to each planned sample position were sequentially magnified and scrutinized. If an artefact was observed for a particular stain and position, the corresponding histological index was treated as missing data. Similarly, if an MR parameter was not defined according to Table 2 for a particular sample, it was automatically discarded.

3.7 | Histological indexing

Histological indices were calculated for each sampling position in area units of 250 × 250 μm², *i.e.* dimensions similar to the in-plane resolution of the MR experiments. The HE segmentation was based on previously presented principles.[19] In brief, a normalization algorithm was used to account for inconsistencies in the preparation and staining process. Normalized images were converted to grey-scale intensity images and subjected to a modified watershed segmentation to detect cell shaped objects (round to oval). Colour thresholding was then used to identify tumour

TABLE 2 MR parameter definitions

| Parameter		Description
Diffusion weighted imaging (DWI)		
		Intravoxel incoherent motion (IVIM)
		$S(b) = S_0(1 - f) \cdot e^{-bD} + S_0 f \cdot e^{-b(D+D^*)}$
		S_0: Signal without diffusion weighting
		A voxelwise Bayesian method with uniform prior distributions and mode as central tendency measure was used to estimate the model parameters[17]
		Parameter limits were D: [0, 5] μm^2/ms, f: [0, 1], D^*: [0, 1000] μm^2/ms, S_0: [0, 2 × S_{max}], where S_{max} is the maximum measured signal
D	Diffusion coefficient	The tissue water diffusion coefficient
D*	Pseudo diffusion coefficient	Perfusion related pseudo diffusion coefficient of incoherently flowing blood in the tissue
f	Perfusion fraction	Signal fraction of from incoherently flowing blood in the tissue
		Apparent diffusion
		$S(b) = S_0 e^{-b \cdot ADC}$
		S_0: Signal without diffusion weighting
		ADC was estimated from a least squares fit with two b-values (0 and 800 s/mm^2)
ADC	Apparent diffusion coefficient	The apparent diffusion coefficient, which includes effects from both diffusion and perfusion
Relaxation time mapping		
		T2* relaxation
		$S(TE) = A + Ce^{\frac{-TE}{T2^*}}$
		S (TE) is the signal intensity for echo time TE
		A = signal bias
		C = signal intensity without T2* relaxation and no bias
		Least squares fitting was used to estimate $T2^*$. Voxels with the goodness-of-fit parameter $R^2 < 0.4$ were excluded
T2*	T2* time	Transversal tissue relaxation time
		T1 relaxation
		$S(TR) = A + C\left(1 - e^{\frac{-TR}{T1}}\right)$
		S (TR) = signal intensity for repetition time TR
		A = signal bias
		C = signal intensity after complete T1 relaxation with no bias
		Least squares fitting was used to estimate $T1$
T1	T1 time	Longitudinal tissue relaxation time
Dynamic contrast enhancement (DCE) MRI		
		Semi quantitative characteristics
		$S(t)$, a continuous representation of signal intensity as a function of time, was determined by fitting a smoothing spline (smoothing parameter = 0.01)
		S_0, the baseline signal intensity, was defined as the mean of the pre-contrast dynamics
		σ_{voxel}, the voxel noise, was defined as the standard deviation of the residuals of $S(t)$ for each voxel
		$S(t) > S_0 + 5 \cdot \sigma_{voxel}$ defined significant contrast enhancement
		σ_{image}, the image noise, was defined as the mean of σ_{voxel}
		$S_0 > 5 \cdot \sigma_{image}$ defined the threshold for inclusion of voxels in the analysis
		S_{max} was defined as the maximum value of $S(t)$ for each voxel
AT	Arrival time	Time after injection required for signal intensity to reach significant enhancement
TOP	Time of peak intensity	Time after injection required to reach maximum signal intensity
TTP	Time to peak	Time between AT and TOP
SEmax	Relative, maximum signal enhancement	Maximum signal intensity relative to baseline signal intensity: $(S_{max} - S_0)/S_0$
SE60	Relative signal enhancement at 60 s	Signal intensity at 60 s after injection relative to signal baseline intensity: $[S(60 s) - S_0]/S_0$
SER	Signal enhancement ratio	Ratio of early (55 s) and late (300 s) relative signal enhancements
CER	Contrast enhancement ratio	Ratio of maximum signal intensity and baseline signal intensity: S_{max}/S_0 Missing value if no significant enhancement was obtained
AUCn	Normalized area under the curve	Area under $S(t)$ between 0 and 5 minutes, normalized to S_0
WI	Wash in	Maximum time derivative of $S(t)$ between AT and TOP
WO	Wash out	Maximum negative time derivative of $S(t)$ between TOP and the last dynamic. Missing value if <5 dynamics left after TOP
BE	Brevity of enhancement	Time between the time points of WI and WO
IS	Initial slope	Average rate of signal enhancement between TOP and contrast injection: $(S_{max} - S_0)/TOP$
NS	Negative slope	Average rate of signal decrease between TOP and the last dynamic. Missing value if <5 dynamics left after TOP
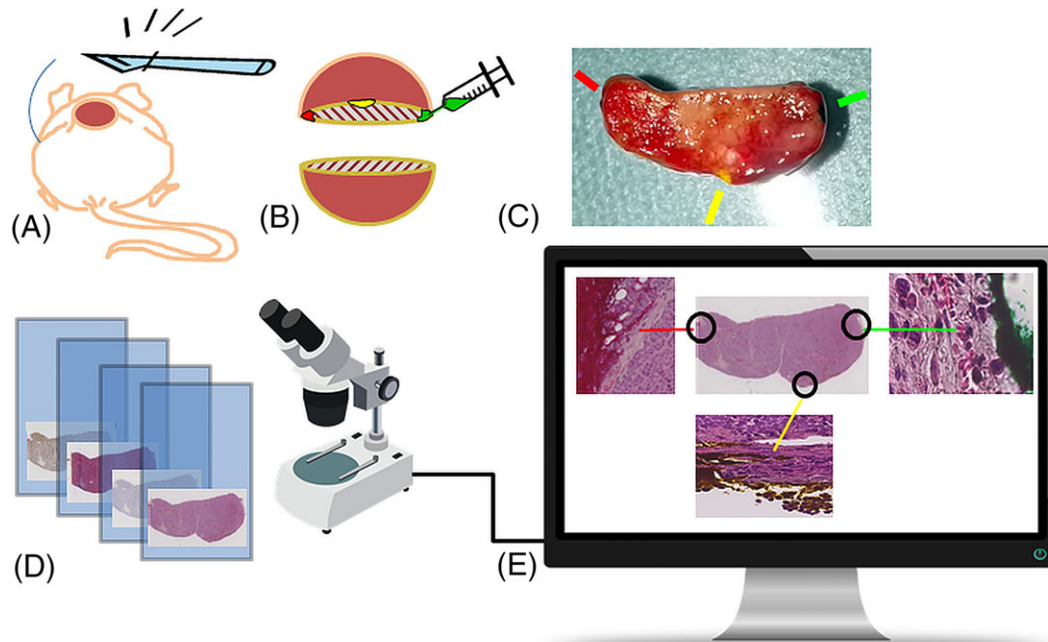
FIGURE 1 Obtaining digital histology images for alignment with the corresponding MR parameter maps. A) The dead animal is positioned for incision through skin and tumour, with scalpel cutting adjacent and parallel to the imaged tumour plane. B) Colour coding of the imaged tumour plane by tissue ink injections on the left, right and dorsal tumour borders. C) Digital photography of the divided and colour coded tumour, with indications of where the ink is visible. The plane of the surface facing the camera will be parallel to the microtome knife sweep plane. D) Glass microscopy slides with differently stained parallel sections are digitized using a slide scanner. E) The ink, preserved through the preparation and paraffin embedding procedure, is visible on the magnified portions of the digitized HE stained section, and can be used to recover the orientation of the histological sections for alignment with the MR images

cells with dark stained nuclei. Assuming that the dark stain represented condensed chromatin due to apoptosis (*c.f.* Kroemer et al. 2005[20]), the apoptotic tumour cell count (HEcount) was defined as the number of apoptotic cells per area unit.

Ki67 positive tumour cells were identified using the method described for HEcount except normalization, which was unnecessary due to the higher contrast between cells and background tissue. The colour threshold was set to detect only cells with brown-stained Ki67 positive chromatin. Proliferating tumour cell count (Ki67count) was thus defined as the number of Ki67 positive cells per area unit.

Micro-vessel density (MVD) and fibrotic density (FD) were determined by colour thresholding only, and defined as the fraction of CD31 and MT positive area per area unit, respectively.

The segmentation and indexing performance was validated by a board-certified pathologist (ON). Examples are shown in Figure 3.

3.8 | Data collection & statistics

All data analyses and statistical tests were performed in MATLAB.

Non-normally distributed MR parameters or histological indices were transformed to approximately normal distributions using the Box-Cox power transformation (MATLAB *boxcox* function).

A linear mixed-effects model including intercept and slope for both fixed and random effects was used to investigate the pairwise correlations between each MR parameter and histological index, where tumour number (1-5) accounted for random effects, such as differences in tissue preparation, staining concentration, colour thresholding, and coil configuration. Observations containing missing values in the pairwise comparisons were omitted. A p-value $<5.0 \times 10^{-4}$ (0.05 adjusted for multiple comparisons) for the fixed effects variable was considered statistically significant.

A statistically significant correlation was further evaluated on a per-animal basis. Five-fold cross-validation of a simple linear regression model between the MR parameter and the histological index was calculated, and the mean squared error of the cross validation, normalized to the squared mean of the histological index, was used to indicate the predictive power of the correlation. The normalization enabled comparison between histological indices.

To study similarities and differences between histological indices and MR parameters, agglomerative hierarchical clustering was performed on the normalized parameters, omitting observations containing missing values. The single linkage distance measure was evaluated due to its invariance to transforms.[21]
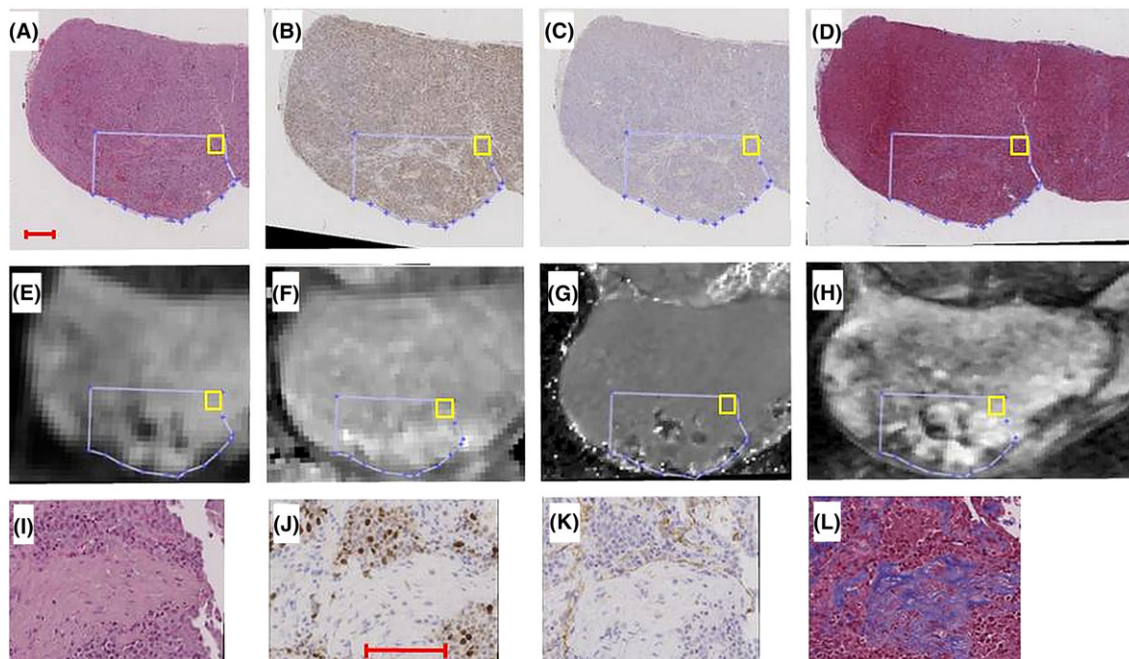
FIGURE 2 Histological images [(A-D): HE, Ki67, CD31, MT] and MR images/parametric maps [(E-H): IVIM-DWI of b = 600 s/mm^2, T1 map, T2* map, T2 weighted image] of tumour 2. The sequential image registration and data sampling procedure is as follows: 1) a tumour sub-region (blue delineation on (A-H)) is intermutually registered on the histological images, 2) the MR parameter maps of the same region are registered to the T2-weighted image (H), 3) the final transformation linking all images to each other is established by registering a histological image also to the T2-weighted image, and 4) a data sampling algorithm systematically extracts data from the entire registered region, before the next tumour sub-region is manually registered for sampling. The yellow rectangle in (A-H) shows the position of a first 250 × 250 μm^2 sample in a registered tumour sub-region. The average MR parameter values in the sample region are extracted from each parameter map, and the histological indices are calculated for the same position. The next sample is then taken adjacent to the first position, and the procedure is repeated until the entire registered region has been sampled. Enlargements of the sample position shown in (A-D) are shown in (I-L). enlargements were used to validate proper registration based on the tissue microscopic landmarks (e.g. region with low cell density on (I-L)), as well as to reject samples where the magnification revealed histological artefacts, such as cracks or folds. Bars in (A) and (J) indicate 1.0 and 0.1 mm, respectively

4 | RESULTS

4.1 | Image quality and registration performance

In general, the 19 MR-derived tissue parameters that were evaluated (Table 2) produced parametric images of good quality, except for the IVIM pseudo diffusion coefficient D^*, which was mostly assigned either of the parameter limit values in the fitting procedure (Table 2). The results based on D^* are thus inconclusive.

The image quality of the MR technique most sensitive to image distortions (EPI-based DWI for estimation of ADC, D, D^* and f) is shown for tumour 2 in Figure 2. The figure confirms visually that the sub-regions in the MR images and histological sections were well aligned after image registration.

4.2 | Tissue segmentation and histological indexing

Results from the automatic segmentation of histological images used for index calculation are shown for tumour 4 in Figure 3. The combination of the algorithm for cell detection and colour thresholding facilitated automatic identification of apoptotic cells in the HE images (Figure 3d) and proliferating cells in the Ki67 images (Figure 3f). Fibrotic tissue (Figure 3h) and vascular endothelial cell presence (Figure 3j) were also adequately identified in the MT and CD31 images, respectively.

Heat maps of the histological indices HEcount, Ki67count, MVD and FD reveal highly heterogeneous and markedly different patterns in the contiguous tumour sections (Figure 3k), which demonstrates a broad range of biological states in the treated tumours.

The distribution of histological indices is shown for each tumour in Figure 4. With some exceptions, there seems to be less variation of indices between tumours than within tumours.
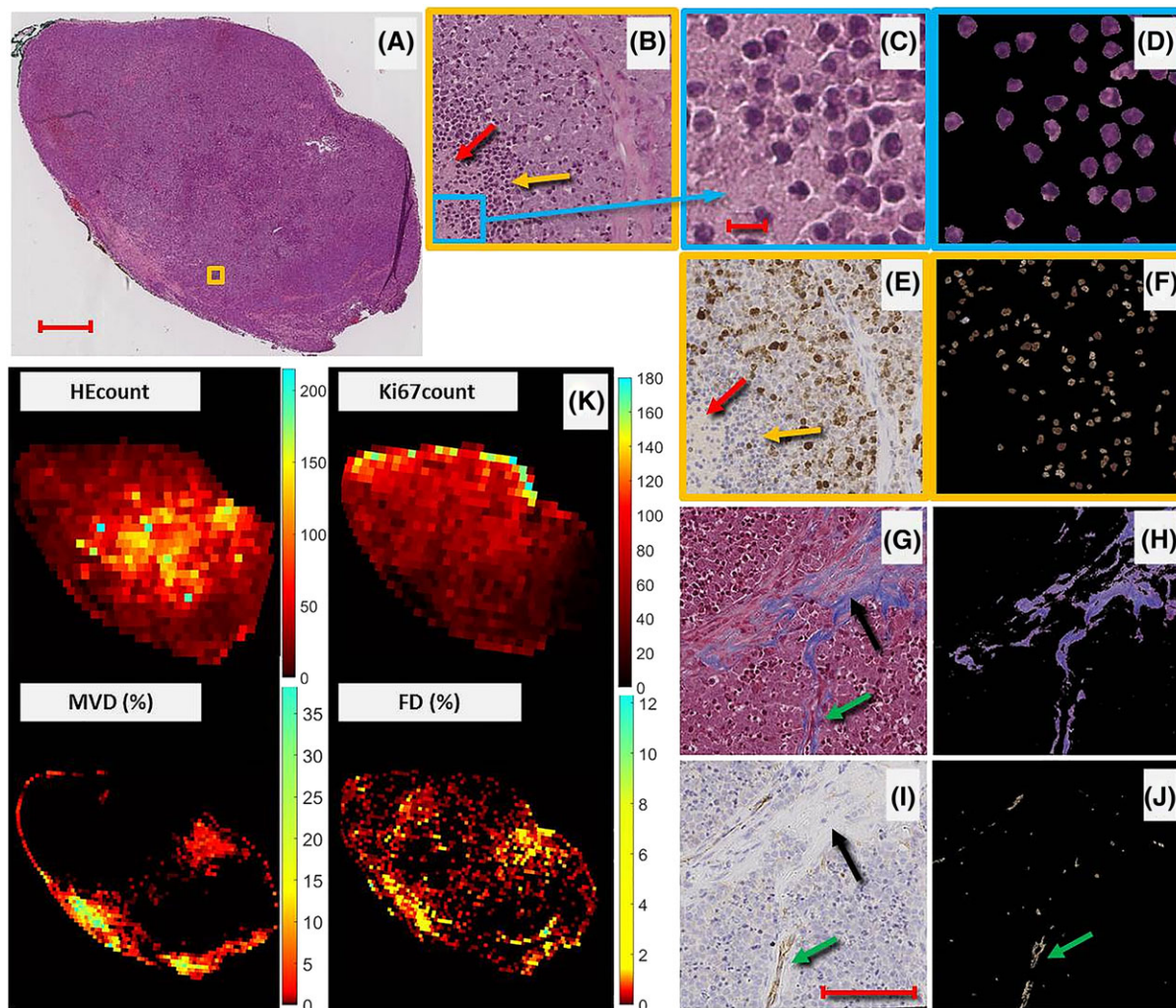
FIGURE 3 Tissue segmentation and calculation of histological indices. (A) HE stained histological section of tumour 4 with corresponding heat maps (K) of HEcount, Ki67count, MVD and FD. The orange square in (A) is magnified in (B), showing apoptotic regions (densely packed, dark stained nuclei of apoptotic cells, indicated by a yellow arrow), necrotic tissue (red arrow) and viable tumour, as verified by the corresponding Ki67 magnification (brown-stained cells in (E)). the region in the blue rectangle in (B) is magnified in (C), where haematoxylin positive (dark purple) nuclear fragments of pyknotic (apoptotic) cells are visible. Another region of the same tumour, but stained with MT, is magnified in (G), with a black arrow indicating fibrotic tissue. The corresponding region stained with CD31 (i) reveals formations of blood vessels by the presence of endothelial cells (brown regions indicated with a green arrow). The right panel of the figure (d, f, h, j) shows the results from the segmentation used for index calculations, resulting in indices: HEcount = 395, Ki67count = 136, FD = 12.3% and MVD = 0.7% in b, f, h and j, respectively. Bars in (A, C, I) indicate 1.0, 0.01 and 0.1 mm, respectively

4.3 | Regression analysis

In total, n = 1821 samples could be extracted from the five evaluated tumours (n = 215, 998, 228, 252 and 128 samples from tumours 1–5, respectively). The HEcount index was excluded completely from the samples of tumour 2 due to a digitization artefact visible on magnification, and the DCE-MRI and $T1$ parameters were excluded from the tumour 3 samples since no adequate landmarks for registration could be identified. Some MR parameters were excluded from analysis since they were undefined according to Table 2 (*e.g.*, if significant contrast enhancement was not reached). A complete overview of the data finally included in the analyses is presented as supplemental material.

The predictive power of simple linear regression models of the pairwise combinations of MR parameters and histological indices that were significantly correlated on the total sample population level are shown in Figure 5. For the set of evaluated MR parameters, we found a relatively high predictive power for correlations with HEcount and Ki67count, and an intermediate level for MVD. FD seems to be the histological index that is most difficult to evaluate *in vivo* using the MR parameters included in this study.

The results from the linear mixed-effects regression analysis of the total sample population are summarized in Figure 6, and the tumour origin and number of samples from each tumour are shown for each correlation in the supplemental figure. Several combinations of MR parameters and histological indices were correlated on a statistically significant level. Of these, the MR parameters that correlated with HEcount were: time of peak intensity (*TOP*, n = 573 samples, regression coefficient (r) = −0.16, p-value (p) = $1e^{-4}$); time to peak (*TTP*, n = 564, r = −0.19, p = $7e^{-6}$); brevity of enhancement (*BE*, n = 563, r = −0.16, p = $1e^{-4}$). MR parameters correlating with Ki67count were: initial slope (*IS*, n = 1355, r = 0.25, p = $1e^{-9}$); T1
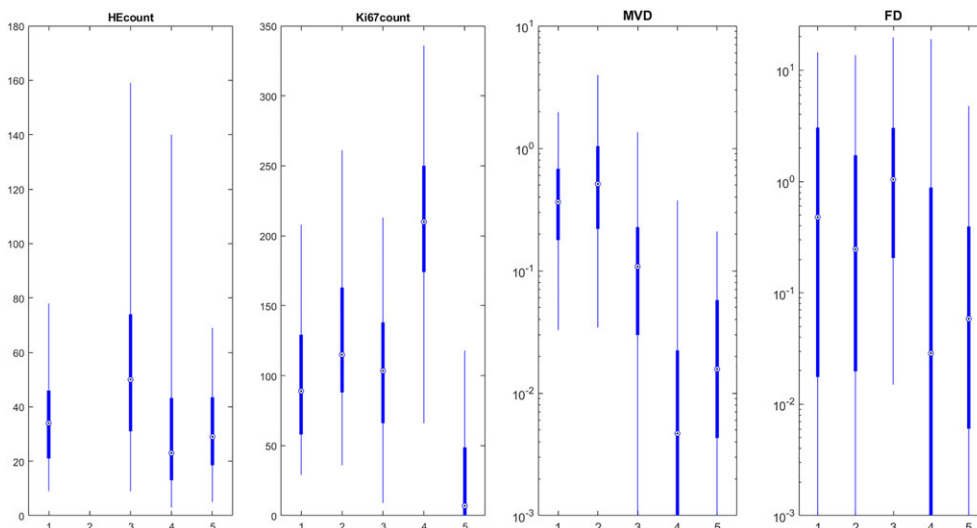
FIGURE 4 Distribution of histological indices within each tumour (x-axis) for the four evaluated stains. By visual inspection, the variation of histological indices within tumours appears greater than the variation between tumours, except for, e.g., MVD in tumour 4 and Ki67count in tumour 4 and 5. The indices of tumour 2 (harvested day 1 after therapy) show a distribution similar to the other tumours. Note the logarithmic scale for improved visualization of MVD and FD indices. The number of indices in the HEcount boxplots for tumour 1–5 are n = 209, 0, 222, 247, and 117, respectively. The corresponding numbers for Ki67count are: 210, 997, 222, 247 and 128; MVD: 213, 997, 222, 247 and 127; FD: 212, 996, 222, 247 and 125. The dot represents the median value, box edges represent 25th and 75th percentiles and whiskers represent 2.5^{th} and 97.5^{th} percentiles
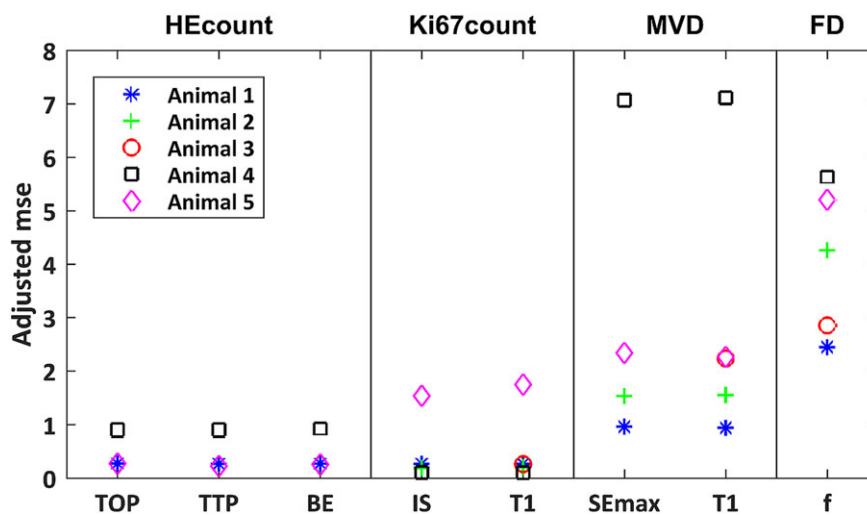

FIGURE 5 Predictive power of pairwise correlations for individual animals. The predictive power, defined as the mean squared error of 5-fold cross validation normalized to the squared mean of the histological index, of models constructed from pairwise simple linear regression of MR parameters and histological indices. Data from each investigated tumour (animal) is shown separately

time ($T1$, $n = 1804$, $r = -0.09$, $p = 4e^{-4}$). MR parameters correlating with MVD were: maximum signal enhancement ($SEmax$, $n = 1583$, $r = -0.10$, $p = 1e^{-4}$); T1 time ($T1$, $n = 1806$, $r = -0.09$, $p = 6e^{-4}$). The MR parameter correlating with FD was the perfusion fraction (f, $n = 1802$, $r = 0.09$, $p = 3e^{-4}$). The corresponding sample statistics for non-significant correlations can be found in the supplemental material.

No obvious clustering was found between the histological indices in the cluster analysis, except for a slightly earlier joining of MVD and FD at approximately 75% of the height of the clade joining all indices (Figure 7, upper dendrogram). The corresponding dendrogram for the MR parameters (Figure 7, lower dendrogram) show that the contrast enhancement ratio (CER) and SEmax, as well as D and ADC, contain highly similar information, as expected from similarities in the parameter definitions. Viewed from a perspective of differences (from above in Figure 7), seven overall groups of parameters may be identified: four groups containing single parameter (wash out (WO), negative slope (NS), T1 and T2*), one group with the IVIM perfusion parameters (f, D^* and $f \times D^*$), one group with the diffusion parameters (D and ADC) and one group with the remaining DCE-MRI parameters.

5 | DISCUSSION

In this work, we demonstrate the potential of multiparametric MRI to non-invasively characterize tumour tissue treated with ^{177}Lu-octreotate therapy. Previous studies that have evaluated MR-derived tissue parameters with histology have focussed on one or a few MR parameters,
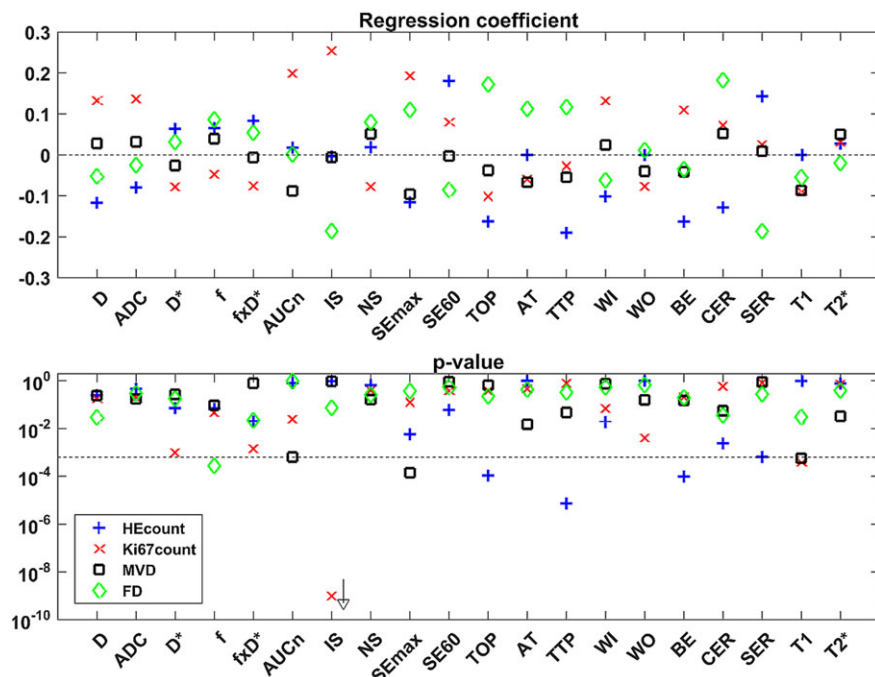
FIGURE 6 Regression coefficients and p-values for correlations found by the linear mixed-effects model. The relation between MR parameters and histological indices, determined for the combined data from all tumour samples (n = 1821) is shown by the regression coefficient (upper plot). The corresponding p-value is shown in the lower plot, where the vertical dashed line indicates the $p = 0.05$ level after adjustment for multiple comparisons. The p-value for IS vs. Ki67count was 1.5e-23. Note that interpretation of D* correlations should be avoided due to poor quality of data
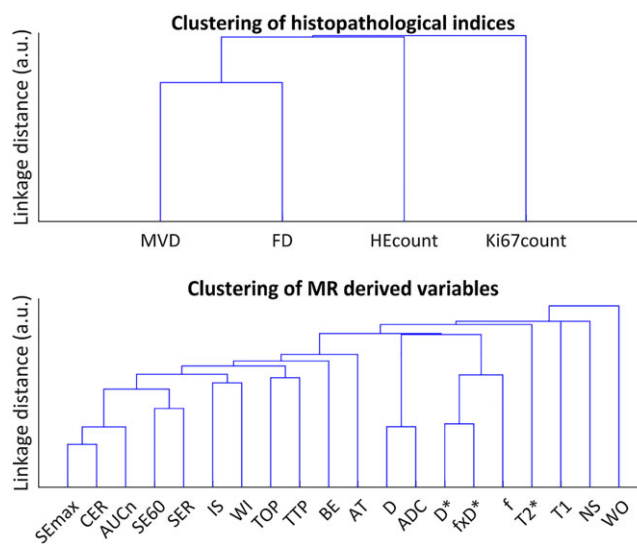

FIGURE 7 Dendrogram of the cluster analysis of the histological indices (upper), and MR derived parameters (lower)

and compared global, averaged tumour MR parameters or histological parameters to address the image registration problems that arise due to deformation of tissue on histological preparation.[9,10,12] We use a semi-automatic method to calculate histological indices on a large number of tissue samples, and use a straightforward method based on registration of tumour sub-regions to accomplish localized correlation analysis.

No standard for spatial registration of histological tissue sections to *in vivo* image data has emerged, but some methods have been proposed.[22,23] Most of them are in-house developments with, *e.g.*, moulding of subcutaneous tumours or stereotactic assemblies and fiducial markers that preserve spatial orientation throughout the histological preparation. Various image registration techniques, such as rigid or affine and elastic registration have been proposed.[24] Unfortunately, the laborious nature common to all techniques effectively restricts their use to smaller studies.

We chose to perform the study on mice xenografted with a patient-derived small-intestine neuroendocrine tumour (GOT1[15]) treated with ^{177}Lu-octreotate, since we have plenty of experience working with this model. The model tumour retains most of the properties of the patient's tumour. In general, we do not expect the choice of treatment to influence the overall results in the present study. It is, however, likely that RNT and, *e.g.*, external radiation therapy would affect the tumour differently due to inhomogeneous vascular supply, resulting in uneven accessibility for RNT.

The primary mechanism of action of radiotherapy is to damage tumour cell DNA. In addition, radiation affects several mechanisms in the tumour microenvironment, including proliferation, vascularization, and tissue degeneration. The results from the linear mixed-effects regression

indicate that it is possible to non-invasively characterize these effects using mpMR, since all four evaluated histological indices could be predicted by one or several MR parameters (Figure 6).

DCE-MRI parameters reflecting exchange rate and perfusion (*e.g.* TTP, TOP and BE) were, to a larger extent than contrast amount-related parameters (*e.g.* AUCn and SEmax), negatively associated with HEcount. These findings match those of other studies[25,26] (Figure 6). If low TTP, TOP, and BE imply adequate vascular function and perfusion, and thereby delivery of ^{177}Lu-octreotate, increased apoptotic activity in the affected regions can be inferred. It should be noted that TTP, TOP, and BE were measured a week prior to the tumour extraction for HEcount calculation, but it seems plausible that apoptosis was induced in tumour regions that previously were well perfused, and thereby adequately reached by the therapeutic agent. Our study also showed a positive correlation between IS, *i.e.* the initial slope of the TIC, and Ki67count. In tumours, the vascular permeability is often high, and IS is therefore considered a measure of perfusion.[27-29] This agrees with our results, since perfused tumour regions should exhibit higher proliferative activity due to adequate supply of nutrients and oxygen. For similar reasons, IS may also reflect tissue oxygen status. In a rat model of prostate cancer, rapid rise of the TIC (similar to high IS) was found in tumour regions that were less hypoxic on histology and *vice versa*.[30] Tissue hypoxia is associated with malignant progression, metastatic potential, angiogenesis, and increased interstitial fluid pressure (IFP),[1,29,31] which makes IS a highly interesting, non-invasive biomarker for tumour response assessment.

The linear models of the functional DCE-MRI parameters (TOP, TTP, BE, IS) predicted the histological indices with relatively high power (Figure 5), which supports the assumption of fairly linear relationships. Furthermore, the cluster analysis (Figure 7) shows that the parameters contain relatively unique information within the largest DCE-MRI cluster (AT and left, Figure 7), underlining the importance of extracting multiparametric information in evaluations of tumour tissue.

Tissue T1 was negatively correlated with both MVD and Ki67count (Figure 6). T1 is affected by variations in macromolecular concentration, and increased MVD is often associated with angiogenesis and high microvascular permeability in tumours.[32-34] Plasma proteins leaking into the extracellular extravascular space (EES) and accumulating due to inadequate lymphatic drainage may thus have reduced T1. Increased biosynthesis of macromolecules related to proliferation may have had the same effect. This finding is consistent with T1 increases that have been observed after vascular normalization induced by anti-angiogenic drugs.[7,31,35] For example, T1 increased when microvascular density and proliferation (determined from CD31 and Ki67 staining, respectively) decreased in a mouse model of ovarian adenocarcinoma receiving anti-angiogenic therapy.[7]

Angiogenesis/MVD and proliferation are clinically relevant tumour characteristics, which makes T1 highly interesting as a non-invasive imaging biomarker that should be further studied. Furthermore, T1 had relatively high predictive power for Ki67count and, unlike IS, T1 would not require contrast injection for Ki67count assessment. Nevertheless, T1 and IS contain complementary information as shown by the cluster analysis (Figure 7). Indeed, T1 reflects an environmental characteristic rather than a functional perfusion-related characteristic, and both parameters may be useful in a multiparametric approach for tumour tissue characterization.

Tissue T2* did not correlate with any of the histological parameters in the present study. T2* is sensitive to magnetic field inhomogeneities caused by, *e.g.*, deoxyhaemoglobin concentrations, and it has also been associated with necrosis.[22] It may, however, be problematic to study T2* correlations with parameters acquired after a certain delay (*e.g.* between imaging and subsequent tissue fixation) due to temporal variations in tissue oxygenation, a phenomenon often observed in solid tumours.[36] It is also possible that CD31-based MVD, the parameter we anticipated would correlate with T2*, is a poor choice for assessing regional perfusion properties, and thereby oxygen status in tumours.

No correlations were found between diffusion parameters (D and ADC) and the evaluated histological indices in this study. Diffusion is affected by the size and viscosity of the EES, membrane structures in cellular debris, and other factors. Although viscosity may not be reflected by any of the evaluated indices, it seems plausible that the level of apoptosis, proliferative activity, or fibrosis should be reflected in Ki67count, HEcount, or FD. Due to the lack of landmarks for registration in central parts of the tumours, however, a majority of the data is based on more peripheral parts of the tumours (typically outside half the tumour radius). Reduced variation of the evaluated parameters may thus have obscured correlations. More likely, however, only day 1 and 13 after therapy were evaluated, so transient or increased effects affecting diffusion may have been missed.

The perfusion fraction (f) showed a significant correlation with the fractional tissue area of fibrosis (FD). Tissue response to irradiation may result in fibrotic tissue formation, and the GOT1 tumour model has demonstrated fibrosis in response to ^{177}Lu-ocreotate therapy, as seen on MT staining.[16,37] Few studies have correlated f with fibrosis in tumours. Residual lesions demonstrated significantly higher f in post-chemoradiotherapy fibrosis compared with untreated tumours in nasopharyngeal carcinoma patients,[38] which is consistent with our results, but opposite correlations have been demonstrated in liver fibrosis.[39] The role of f in tumour characterization thus remains unclear, and further efforts to optimize acquisition and post-processing methods for IVIM-DWI are probably required before f, as well as D*, can be properly understood and evaluated.

The heat maps of the histological indices (Figure 3k) are informative regarding the heterogeneity of the tumour vasculature and viability. As previously mentioned, the use of CD31-based MVD as a measure of vascular functionality and perfusion may not be optimal. MVD is mostly seen in the tumour periphery, whereas apoptosis and proliferation seem more evenly distributed throughout the tumour (Figure 3k), both of which would require vascular supply. A measure of the functional properties or maturity of the vasculature, instead of a static measure of endothelial cell presence (MVD), may better reflect perfusion.[32-34]

Some potential limitations of this study should be noted. 1) Some correlations may have been obscured by the temporal discordance between DCE-MRI experiments (day 8) and tissue extraction (day 13) in 4/5 tumours. It is likely that the tumour biological characteristics evolved between day 8 and 13, which may have led to false negative results, *i.e.* reduced or missed correlations. However, more than 50% of the data were from

tumour 2, imaged and harvested on the same day. 2) The analyses were based on data from five tumours only. This was partly due to the index calculations requiring lengthy data processing due to the immense amount of data associated with digitized histological images of microscopic resolution. Furthermore, our own tumour inclusion criteria, namely high image quality, minimal artefacts on histological sections, and adequate landmarks for proper image registration, restricted the number of tumours for evaluation. However, the variation of indices within tumours seems greater than the variation between tumours with some exceptions (Figure 4), which indicates that additional tumours would add little information. 3) As mentioned above, a lack of landmarks in central tumours reduced the amount of data from those regions, which may have limited the range of biological characteristics evaluated. To address this problem, other methods to ascertain proper registration are required. 4) No quantitative evaluation of registration accuracy was made in this study, and the landmark-based approach for image registration entails a risk of introducing false correlations. A more objective approach would be to use non-lesion features, such as markers outside the tumour, but intra-tumour registration may be degraded by such an approach. 5) The 2D representation of the tumour tissue provided by the histological sections makes the method insensitive to tumour heterogeneity in the dimension of the MR slice thickness. Since biological features investigated can be seen to vary even along the dimensions of a sample (*e.g.*, Figure 3), it is obvious that variations along the distance of an MR slice (4 times the sample dimensions) will influence the accuracy of the index calculations. A possible remedy would be to collect more histological sections within the distance covered by the MR slice, with enough separation to get a better representation of the imaged tumour tissue. For this to improve the accuracy, however, would require better knowledge of the precise location of the beginning and end of the acquired image slice, and thus a more sophisticated system for tracking those locations than offered by manual application of tissue ink or similar fiducial markers. There are also substantial processing times and costs involved in histological processing and post-processing of the digitized images that would have to be considered.

6 | CONCLUSIONS

In this work, MR parameters are correlated with spatially registered histological parameters of the imaged tumour tissue. Registration problems due to MR artefacts or morphologically distorted histological sections were minimized by sequential registration of tumour sub-regions, and objective evaluation on a substantial amount of data samples by statistical regression methods was enabled by the supervised automatic histological indexing method.

Predictive power and statistical significance were high for several of the correlations found between MR parameters and histological indices. Models predicting HEcount and Ki67count had the strongest predictive power, while models describing MVD and FD had slightly lower predictive power. Altogether, HEcount could be predicted by three DCE-MRI parameters related mainly to perfusion (*TOP*, *TTP*, and *BE*); Ki67count could be predicted by one DCE-MRI parameter (*IS*, reflecting perfusion) and one relaxation parameter related to macromolecular content (*T1*); MVD could also be predicted by *T1*, and by a DCE-MRI parameter reflecting the amount of contrast reaching the tissue (*SEmax*); and FD could be predicted by one IVIM-DWI parameter reflecting fractional volume of actively perfused tissue (*f*). In total, seven of the evaluated MR parameters were capable of predicting apoptosis, proliferation, vessel density or fibrosis in the studied tumour type. Apart from the similarly defined *TOP* and *TTP*, the data provided by these MR parameters seem, based on cluster analysis, to contain unique information.

This work demonstrates the importance of combining data from several MR methods for gaining knowledge of tumour tissue characteristics, and we believe the information contained in this work will be valuable for further studies on mpMR evaluation of tumour tissue and response assessment. Further work is needed, such as improvements of registration procedures and MR post-processing methods.

ORCID

Mikael Montelius 🔢 https://orcid.org/0000-0001-9103-3446

REFERENCES

1. Figueiras RG, Padhani AR, Goh VJ, et al. Novel oncologic drugs: what they do and how they affect images. *Radiographics*. 2011;31(7):2059-2091. https://doi.org/10.1148/rg.317115108

2. Eisenhauer EA, Therasse P, Bogaerts J, et al. New response evaluation criteria in solid tumours: revised RECIST guideline (version 1.1). *Eur J Cancer*. 2009;45(2):228-247. https://doi.org/10.1016/j.ejca.2008.10.026

3. Therasse P, Arbuck SG, Eisenhauer EA, et al. New guidelines to evaluate the response to treatment in solid tumors. *Clin Trials*. 2005;12(3):16-27.

4. Montelius M, Spetz J, Jalnefjord O, et al. Identification of Potential MR-Derived Biomarkers for Tumor Tissue Response to[177]Lu-Octreotate Therapy in an Animal Model of Small Intestine Neuroendocrine Tumor. *Transl Oncol*. 2018;11(2). https://doi.org/10.1016/j.tranon.2017.12.003

5. Knopp MV, von Tengg-Kobligk H, Choyke PL. Functional magnetic resonance imaging in oncology for diagnosis and therapy monitoring. *Mol Cancer Ther*. 2003;2(4):419-426.

6. Le Bihan D, Breton E, Lallemand D, Aubin ML, Vignaud J, Laval-Jeantet M. Separation of diffusion and perfusion in intravoxel incoherent motion MR imaging. *Radiology*. 1988;168(2):497-505. https://doi.org/10.1148/radiology.168.2.3393671

7. Ravoori MK, Nishimura M, Singh SP, et al. Tumor T1 relaxation time for assessing response to bevacizumab anti-Angiogenic therapy in a mouse ovarian Cancer model. *PLoS One*. 2015;10(6):e0131095. https://doi.org/10.1371/journal.pone.0131095

8. Heijmen L, Ter Voert EEGW, Oyen WJG, et al. Multimodality imaging to predict response to systemic treatment in patients with advanced colorectal cancer. *PLoS One*. 2015;10(4):1-13. https://doi.org/10.1371/journal.pone.0120823

9. Moestue SA, Huuse EM, Lindholm EM, et al. Low-molecular contrast agent dynamic contrast-enhanced (DCE)-MRI and diffusion-weighted (DW)-MRI in early assessment of bevacizumab treatment in breast cancer xenografts. *J Magn Reson Imaging*. 2013;38(5):1043-1053. https://doi.org/10.1002/jmri.24079

10. Hompland T, Ellingsen C, Galappathi K, Rofstad EK. DW-MRI in assessment of the hypoxic fraction, interstitial fluid pressure, and metastatic propensity of melanoma xenografts. *BMC Cancer*. 2014;14(1):92. https://doi.org/10.1186/1471-2407-14-92

11. Dominietto M, Rudin M. Could magnetic resonance provide in vivo histology? *Front Genet*. 2013;4:1-15. https://doi.org/10.3389/fgene.2013.00298

12. Wegner CS, Gaustad J-V, Andersen LMK, Simonsen TG, Rofstad EK. Diffusion-weighted and dynamic contrast-enhanced MRI of pancreatic adenocarcinoma xenografts: associations with tumor differentiation and collagen content. *J Transl Med*. 2016;14(1):161. https://doi.org/10.1186/s12967-016-0920-y

13. Borren A, Moman MR, Groenendaal G, et al. Why prostate tumour delineation based on apparent diffusion coefficient is challenging: an exploration of the tissue microanatomy. *Acta Oncol*. 2013;52(8):1629-1636. https://doi.org/10.3109/0284186X.2013.787164

14. Hillengass J, Bäuerle T, Bartl R, et al. Diffusion-weighted imaging for non-invasive and quantitative monitoring of bone marrow infiltration in patients with monoclonal plasma cell disease: a comparative study with histology. *Br J Haematol*. 2011;153(6):721-728. https://doi.org/10.1111/j.1365-2141.2011.08658.x

15. Kölby L, Bernhardt P, Ahlman H, et al. A transplantable human carcinoid as model for somatostatin receptor-mediated and amine transporter-mediated radionuclide uptake. *Am J Pathol*. 2001;158(2):745-755. https://doi.org/10.1016/S0002-9440(10)64017-5

16. Dalmo J, Spetz J, Montelius M, et al. Priming increases the anti-tumor effect and therapeutic window of ^{177}Lu-octreotate in nude mice bearing human small intestine neuroendocrine tumor GOT1. *EJNMMI Res*. 2017;7(1). https://doi.org/10.1186/s13550-016-0247-y

17. Gustafsson O, Montelius M, Starck G, Ljungberg M. Impact of prior distributions and central tendency measures on Bayesian intravoxel incoherent motion model fitting. *Magn Reson Med*. 2017. https://doi.org/10.1002/mrm.26783

18. Montelius M, Ljungberg M, Horn M, Forssell-Aronsson E. Tumour size measurement in a mouse model using high resolution MRI. *BMC Med Imaging*. 2012;12. https://doi.org/10.1186/1471-2342-12-12

19. Veta M, van Diest PJ, Kornegoor R, Huisman A, Viergever MA, Pluim JPW. Automatic Nuclei Segmentation in H&E Stained Breast Cancer Histopathology Images. *PLoS One*. 2013;8(7). https://doi.org/10.1371/journal.pone.0070221

20. Kroemer G, El-Deiry WS, Golstein P, et al. Classification of cell death: recommendations of the nomenclature committee on cell death. *Cell Death Differ*. 2005;12:1463-1467. https://doi.org/10.1038/sj.cdd.4401724

21. Hastie T, Tibshirani R, Friedman J. The elements of statistical learning. *Bayesian Forecast Dyn Model*. 2009;1:1-694. https://doi.org/10.1007/b94608

22. Alic L, Haeck JC, Bol K, et al. Facilitating tumor functional assessment by spatially relating 3D tumor histology and in vivo MRI: image registration approach. *PLoS One*. 2011;6(8):1-10. https://doi.org/10.1371/journal.pone.0022835

23. Seise M, Alhonnoro T, Kolesnik M. Interactive registration of 2D histology and 3D CT data for assessment of radiofrequency ablation treatment. *J Pathol Inform*. 2011;2(S9). https://doi.org/10.4103/2153-3539.92036

24. Klein S, Staring M, Pluim JPW. Evaluation of optimization methods for nonrigid medical image registration using mutual information and B-splines. *IEEE Trans Image Process*. 2007;16(12):2879-2890. https://doi.org/10.1109/TIP.2007.909412

25. Bol K, Haeck JC, Groen HC, et al. Can DCE-MRI explain the heterogeneity in Radiopeptide uptake imaged by SPECT in a pancreatic neuroendocrine tumor model? *PLoS One*. 2013;8(10):1-11. https://doi.org/10.1371/journal.pone.0077076

26. Haeck JC, Bol K, de Ridder CMA, et al. Imaging heterogeneity of peptide delivery and binding in solid tumors using SPECT imaging and MRI. *EJNMMI Res*. 2016;6(1):3. https://doi.org/10.1186/s13550-016-0160-4

27. Hoffmann U, Brix G, Knopp MV, Hess T, Lorenz WJ. Pharmacokinetic mapping of the breast: a new method for dynamic MR mammography. *Magn Reson Med*. 1995;33(4):506-514. https://doi.org/10.1002/mrm.1910330408

28. Rudin M. Imaging readouts as biomarkers or surrogate parameters for the assessment of therapeutic interventions. *Eur Radiol*. 2007;17(10):2441-2447. https://doi.org/10.1007/s00330-007-0619-9

29. Li LZ, Zhou R, Xu HN, et al. Quantitative magnetic resonance and optical imaging biomarkers of melanoma metastatic potential. *Proc Natl Acad Sci U S a*. 2009;106(16):6608-6613. https://doi.org/10.1073/pnas.0901807106

30. Cho H, Ackerstaff E, Carlin S, et al. Noninvasive multimodality imaging of the tumor microenvironment: registered dynamic magnetic resonance imaging and positron emission tomography studies of a preclinical tumor model of tumor hypoxia. *Neoplasia*. 2009;11(3):247-259. 2p following 259. https://doi.org/10.1593/neo.81360

31. Jain RK. Normalizing tumor microenvironment to treat cancer: bench to bedside to biomarkers. *J Clin Oncol*. 2013;31(17):2205-2218. https://doi.org/10.1200/JCO.2012.46.3653

32. Knopp MV, Weiss E, Sinn HP, et al. Pathophysiologic basis of contrast enhancement in breast tumors. *J Magn Reson Imaging*. 1999;10(3):260-266. https://doi.org/10.1002/(SICI)1522-2586(199909)10:3<260::AID-JMRI6>3.0.CO;2-7

33. Sorace AG, Quarles CC, Whisenant JG, et al. Trastuzumab improves tumor perfusion and vascular delivery of cytotoxic therapy in a murine model of HER2+ breast cancer: preliminary results. *Breast Cancer Res Treat*. 2016;155(2):273-284. https://doi.org/10.1007/s10549-016-3680-8

34. Bali MA, Metens T, Denolin V, et al. Tumoral and nontumoral pancreas: correlation between quantitative dynamic contrast-enhanced MR imaging and histopathologic parameters. *Radiology*. 2011;261(2):456-466. https://doi.org/10.1148/radiol.11103515

35. Lescher S, Jurcoane A, Veit A, Bähr O, Deichmann R, Hattingen E. Quantitative T1 and T2 mapping in recurrent glioblastomas under bevacizumab: earlier detection of tumor progression compared to conventional MRI. *Neuroradiology*. 2014;57(1):11-20. https://doi.org/10.1007/s00234-014-1445-9

36. Baudelet C, Cron GO, Ansiaux R, et al. The role of vessel maturation and vessel functionality in spontaneous fluctuations ofT2*-weighted GRE signal within tumors. *NMR Biomed*. 2006;19(1):69-76. https://doi.org/10.1002/nbm.1002

37. Kölby L, Bernhardt P, Johanson V, et al. Successful receptor-mediated radiation therapy of xenografted human midgut carcinoid tumour. *Br J Cancer*. 2005;93(10):1144-1151. https://doi.org/10.1038/sj.bjc.6602845

38. Lai V, Li X, Lee VHF, Lam KO, Chan Q, Khong PL. Intravoxel incoherent motion MR imaging: comparison of diffusion and perfusion characteristics between nasopharyngeal carcinoma and post-chemoradiation fibrosis. *Eur Radiol*. 2013;23(10):2793-2801. https://doi.org/10.1007/s00330-013-2889-8

39. Zhang Y, Jin N, Deng J, et al. Intra-voxel incoherent motion MRI in rodent model of diethylnitrosamine-induced liver fibrosis. *Magn Reson Imaging*. 2013;31(6):1017-1021. https://doi.org/10.1016/j.mri.2013.03.007

SUPPORTING INFORMATION

Additional supporting information may be found online in the Supporting Information section at the end of the article.